Koc. J. Sci. Eng., 5(2): (2022) 159-166 https://doi.org/10.34088/kojose.792056

Kocaeli University

Kocaeli Journal of Science and Engineering

http://dergipark.org.tr/kojose

Mapping of Gradient Patterns Generated with Helmholtz Coils for Localized Magnetic Fluid Hyperthermia

Serhat KÜÇÜKDERMENCİ [1, *]

[1] *Department of Electrical and Electronics Engineering, Balıkesir University, Balıkesir, 10463, Turkey,* ***ORCID:*** *0000-0002-6421-7773*

Article Info

Research paper

Received : *September 08, 2020*
Accepted : *April 22, 2022*

Keywords

Cancer Treatments
Field-Free Region
Magnetic Fluid Hyperthermia
Helmholtz Coils
Static Magnetic Field

Abstract

Magnetic fluid hyperthermia (MFH) is a new generation cancer treatment method under development. One of the challenges that arise in the practical applications of MFH is the limited control of magnetic nanoparticles (MNP). In order to overcome this problem, new approaches are being investigated in MFH tests. Localization of MNP oscillations can be achieved through static magnetic field-free region (FFR) and static magnetic field (SMF) gradients generated by permanent magnets or electromagnets. In this study, Helmholtz coils were used as SMF source to generate gradient patterns (GPs). Finite element method simulation was used to predict GPs that would emerge in the study area. An experiment platform was produced in which the GP would be generated with parametric current changes. Measurements were taken when source currents were (1.1, 1.1), (2.2, 2.2), (4.4, 4.4) and (2.2, -2.2) A, respectively. It was observed that FFR form could be manipulated with coil current. The mapping of the GPs and determining FFRs for the use of localized MFH were discussed for the first time in this study. The findings provide insight into which GP is appropriate in which situations in localized MFH.

1. Introduction

Magnetic resonance imaging [1-2], targeted drug delivery technologies [3-4] and magnetic fluid hyperthermia (MFH) [5-6] can be counted as examples of magnetic nanoparticle (MNP) applications interacting with magnetic fields. MFH is a medical procedure in which cancerous cells are brought to a temperature between 42-46 °C with MNPs [7]. When MNPs are exposed to an alternating magnetic field (AMF), the magnetic energy is converted into heat energy with the oscillating movement. Cancerous cells lose their effectiveness with the high temperature in the environment. Inversely, healthy cells are more resistant to heat than cancer cells. The heat generating capacity of MNPs is defined as the specific absorption rate (SAR) and it is expressed by Eq. (1).

$$SAR = c\frac{V_s}{m_{MNP}} \times \frac{dT}{dt} \tag{1}$$

In the formula above, c is the specific heat capacity of the medium, V_S is the volume of the sample, m_{MNP} is the mass of the MNPs, and dT/dt is the time derivative of the temperature difference.

The heat production of MNPs by the AMF effect is explained by the relaxation losses. The deflection motion of MNP moments is defined as Neel relaxation. In Brownian relaxation, MNPs interact with the medium fluid and make a mechanical motion. The Neel and Brownian characteristic relaxation times are expressed as τ_N and τ_B, respectively. The effective relaxation time (τ_{eff}) is given by Eq. (2).

$$\tau_{eff} = (\tau_B.\tau_N)/(\tau_B + \tau_N) \tag{2}$$

One of the models describing the volumetric power density emitted by MNPs exposed to AMF is the Rosensweig model and it is expressed by Eq. (3).

$$P = \pi\mu_0\chi_0 H_{ac}^2 f \frac{\omega\tau}{1+(\omega\tau)^2}[W/m^3] \tag{3}$$

Here, χ_0 is magnetic susceptibility, H_{ac} and f are AMF amplitude and frequency, τ is effective relaxation time and ω is angular frequency, respectively.

* Corresponding Author: kucukdermenci@balikesir.edu.tr

The typical problem in MFH applications is the difficulty of localizing the heat to the tumor without damaging the healthy tissue, considering here is a tendency for MNPs to migrate from the tumor site to healthy tissue during the MFH tests. There are theoretical experimental studies [8-9] that show MNP behaviors under the influence of AMF can be changed by adding static magnetic field (SMF) patterns. If the SMF gradient pattern (GP) is added to the MFH test environment, MNPs may have different SAR values depending on their location. SMF sources are positioned such that the magnetic flux density vectors bend each other. A GP suitable for localized MFH is created. MNPs remaining in the field-free region (FFR) oscillate under the influence of AMF. The oscillations of MNPs under the influence of the SMF gradient are either restricted or completely blocked (see Figure 1).

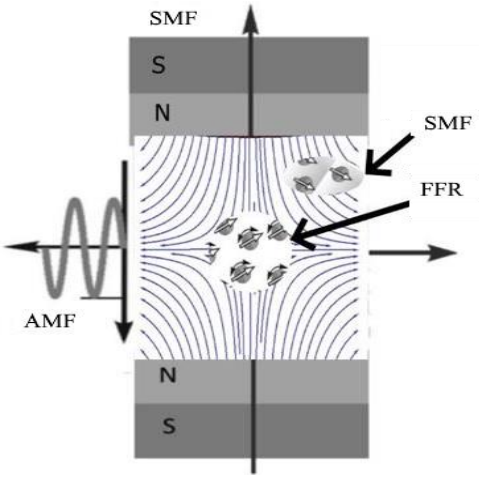

Figure 1. FFR pattern.

Among the studies on MFH, Tasci et al. [10] showed that the MNP temperature rise could be controlled in in vivo MFH experiments with their proposed method. The SMF source made with DC coils was positioned on both sides of the AMF generating coil in their study. SMF gradients surrounding the FFR in the study area were obtained by feeding the coils with equal and opposite DC currents. In another study, Hensley et al. established a system in which permanent magnets were used to focus the heat to the desired area with the help of FFR. The proposed system was capable of performing magnetic particle imaging and MFH operations [11]. In another study, Ma et al. [12] used neodymium iron boron (NdFeB) permanent magnets with dimensions of 40 mm × 40 mm × 20 mm as SMF source in their experiment setup. Magnets were located on both sides of the AMF generating coil. It was reported that MNP samples remaining within the FFR effectively generated heat and the SAR value of MNPs was limited in the static GP.

A brief literature comparison of MFH studies including SMF sources is presented in Table 1. According to the table, magnetic flux direction and intensities of SMF sources can take different values. These studies indicate that both DC current fed coils and permanent magnets can be used as SMF sources. In some experiments opposite SMF poles were placed facing the study area, resulting in magnetic flux vectors supporting each other and completely blocking the MNP oscillations. In other experiments the same SMF poles were placed facing the study area. Consequently, magnetic flux vectors generated FFR in some regions of the study area to allow MNPs to oscillate freely. Mapping of the GP has not been studied in detail in any of these studies.

Table 1. Comparison of MFH studies including SMF sources.

Ref.	SMF source /Intensity	SMF sources / Flux direction	Gradient pattern mapping	FFR measurements
[13]	Permanent magnet / 2,6 mT - 15,4 mT	Single magnet, magnet pair / same direction	-	-
[10]	DC fed coil	A pair / opposite direction	-	-
[12]	Permanent magnet / 5mT - 0.2 T	A pair / opposite and same direction	-	-
[14]	DC fed coil	A pair / same direction	-	-
[15]	DC fed coil	A pair / same direction	-	-
Proposed study	Helmholtz coil	A pair / same direction and opposite direction	Point probe measurements were taken in workspace	FFR major and minor axis measurements and area calculations were done.

Literature comparison of workspaces and target objects are shown in Table 2. Workspaces generally the inner volume of helical shaped work-coil. Ferrofluid containing test tubes and regional tumor masses of small animals can be considered as the target object. Small test tubes can be placed periodically with distance as shown in

Figure 2a. Focusing effect can be applied to test tubes separately or regionally. Another example can be a long test tube containing MNP. This tube may have a length of 47.5 mm and an outer diameter of 9.6 mm. The height and diameter is labelled with letters *A* and *B* in Figure 2b. When this type of tube is placed horizontally, the focusing of FFR can be applied to some parts of the tube. When the target object is the tumor mass in the small experimental animal, targeting FFR is up to the experiment conditions. For instance tumor mass can be in the shape of line-like or surface-like geometries as shown with the letters *L* and *S* in Figure 2c.

Table 2. Specifications of the instrumentation from MNP tests.

Properties of the workspace	Properties of the target objects	Ref.
Radius of the coil ≈ 5 cm Cross-section area of workspace ≈ 78.5 cm^2	One test-tube located in the center of the coil, the radius of the tube, r ≈ 0.5 cm, Target area ≈ 0.785 cm^2	[13]
Radius ≈2 cm, height ≈ 6 cm Cross-section area of workspace ≈ 24 cm^2	Spherical plastic cups, r ≈ 0.2 cm, target area ≈ 0.126 cm^2	[10]
Coil diameter = 3 cm	Two phantoms stay close to the heating region of the coil (20mm).	[12]
Coil with a diameter = 3 cm	Tube diameter = 8 mm, target area ≈ 0.502 cm^2	[14]
Solenoid coil diameter = 4 cm, length = 10 cm. Cross-section area of workspace ≈ 40 cm^2	Spherical core with a radius of 4.9 mm	[15]

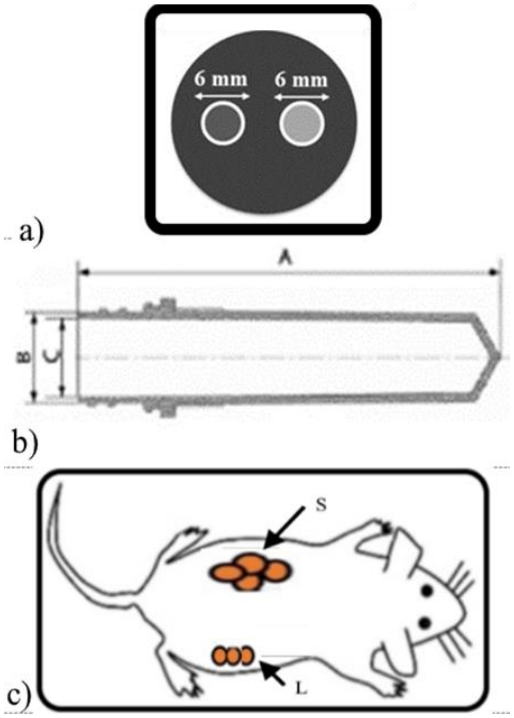

Figure 2. Schematic representation of target objects (a) periodically arranged test tubes, (b) horizontally located test tube, (c) small test animal.

In bioelectromagnetic applications, either current fed electromagnets [16] or permanent magnets [17] are preferred as SMF sources. NdFeB permanent magnets produce stronger magnetic flux density compared to conventional magnets [18]. However, the positions of the magnets must be changed in order to change the magnetic flux patterns in the workspace. Helmholtz coils are a pair of thin, parallel and identical coils separated by a distance. To change the magnetic flux density generated by Helmholtz coils, it is sufficient to change source currents while the coil positions stay fixed. These coils are commonly used to generate highly uniform magnetic fields in the space between the coils. Furthermore, this concept can be reversed to use the coils as gradient source by changing the electric current directions, which allows Helmholtz coils to generate FFR instead of uniform magnetic field for specific purposes like localized MFH. In addition, flux densities can be changed with good resolution by fine-tuning source currents of the coils.

The shape and size of the FFR is very important in studies of localized hyperthermia. The compatibility of FFR with the target object in terms of form and size increases the success rate of protecting healthy tissue from unwanted heating. However, as seen in Table 1, this issue has not been discussed in detail. The aim of this study is to determine FFR properties using gradient pattern mapping and measurements. In various studies, coil or magnet configurations have been used as SMF sources. For the reasons mentioned above, Helmholtz coils were preferred as the SMF source in this study.

2. Materials and Methods

2.1. Simulation Medium

A multiphysics simulation software (COMSOL® Multiphysics, COMSOL AB, Stockholm, Sweden) was used for GP modeling. This software uses finite element analysis method to discretize the computational areas. Simulation medium consists of Helmholtz coils and a target object as shown in Figure 3a. Helmholtz coils used in this study had diameter of 205 mm and 250 turns. The distance between the center of the coils was 144 mm. The target

object was a cylinder with its center of gravity at (-50, 0, 0) mm. It had a radius of 10 mm and 100 mm height. Target object was a representative illustration of a sample tube or a small test animal for in vivo or in vitro tests. The distances of coil centers from the origin were kept fixed at (-72, 72) mm on the x-axis. First, the coils were fed by symmetrical currents to generate FFR. Coil currents (I_1, I_2) for left and right coils were (1.1, 1.1) , (2.2, 2.2) and (4.4, 4.4) A, respectively. Then one of the poles was reversed by changing current direction to generate MNP oscillation blocking effect in all workspaces when coil currents were (2.2, -2.2) A.

2.2. Experiment Setup

The experiment setup consisted of Helmholtz coils, power supplies, experiment platform and measuring area. Helmholtz coils with 182.5 mm average diameter and 30 mm thickness were used. The coils were made of copper wire with 1 mm diameter and 250 turns. The distance between the center of the coils was 144 mm. The power supplies for the coils were indicated by *A* in Fig 3b. The distance could be adjusted without disturbing the alignment by inserting the Helmholtz coil into the sliding parts indicated by *B*. The region indicated by *C* was the workspace where the FFR would be generated and measured. By placing the measurement paper as shown in Figure 3b, a total of 81 measurement points were determined on the x and y axes with 10 mm intervals from -40 mm to 40 mm. A transparent magnetic field indicator plate was placed in the workspace as shown in Figure 3c. This plate contained independent compass arrows arranged in matrix form. With the help of these compass arrows, the poles of the source magnets could be determined visually. The FFR in the middle and SMF gradient around the FFR could be easily detected.

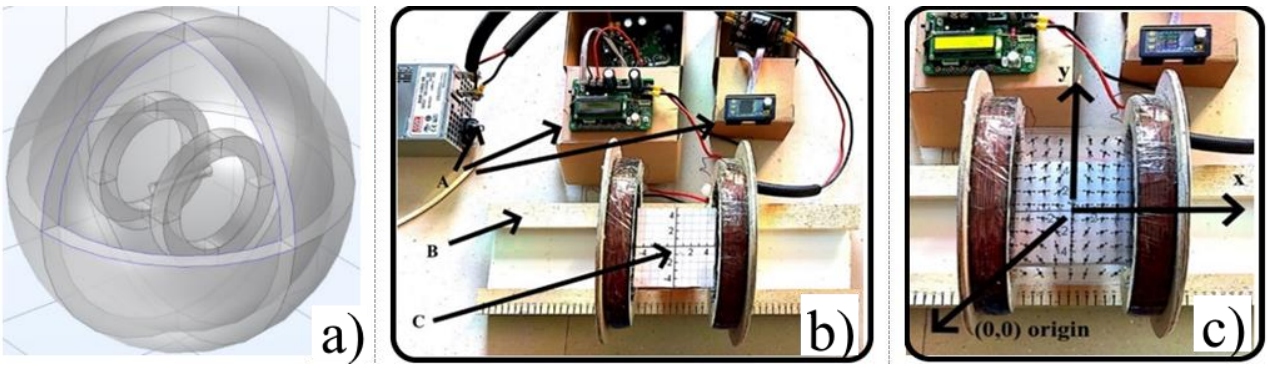

Figure 3. a) simulation medium, b) experiment setup, c) placement of the magnetic field indicator plate.

3. Results and Discussion

3.1. Simulation Results

Magnetic field color maps and arrow representation of flux lines for different current values are shown in Figure 4 a-d, respectively. The FFR form can be manipulated by current change. It was found that the more the current level rose the more the FFR shrunk. To determine the shrinking effect numerically, measurements were done on contour representations of GPs as shown in Figure 5. Conditions of MFH experiments in the literature vary widely. For example, AMF intensity can range from 0.8 to 115 kA/m [19]. Ideally the limit value of SMF can be selected as 10 G (≈0.8 kA/m).

Major axis (MA_1) and minor axis (MA_2) of FFRs were measured. MA_1 and MA_2 were (15.2, 6.7), (6.4, 3.3) and (3.1, 1.8) cm when (I_1, I_2) were (1.1, 1.1), (2.2, 2.2) and (4.4, 4.4) A, respectively. It was found that if current rose to high levels, FFR could transform to a so-called field free point. And FFR could be focused into a very small area. When current applied to coils were (2.2, -2.2) A, there was no FFR occurring in the workspace (see Figure 4d). This uniform field can be used to block MNP oscillations across the entire workspace.

Magnetic flux density measurements were taken at 81 locations spaced 10 mm between -40 mm and 40 mm in the x and y axes. Measurements were taken for four different current values. Point measurement tables in the simulation environment of GPs can be found as a file in the supplementary material.

It was found that FFR can be focused on the target object and its form can be manipulated by changing source current. Point-like or rod-like forms of FFR can be achieved if suitable experiment conditions are provided. Fine tuning of flux densities is also available with coil source currents. FFR ($B \leq 10$ G) areas shown in Figure 5 can be considered as ellipses.

The area of an ellipse *A* can be calculated with semi major axis *a* and semi minor axis *b* by Eq. (4).

$$A = \pi ab \tag{4}$$

When (I_1, I_2) are (1.1, 1.1), (2.2, 2.2) and (4.4, 4.4) A, the lengths *a* and *b* are (7.6, 3.35), (3.2, 1.65) and (1.55, 0.9) cm and surface areas are 79.98, 16.58 and 4.38 cm^2, respectively.

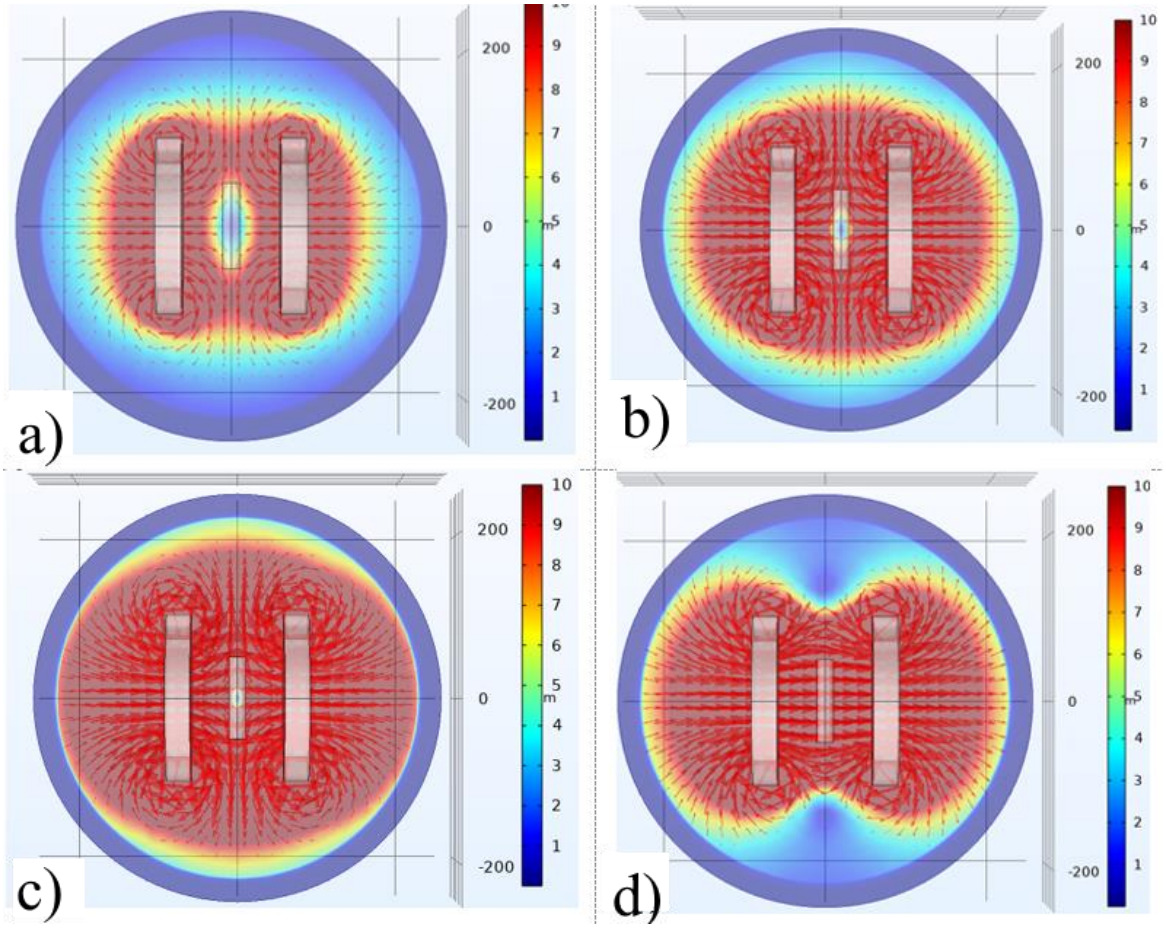

Figure 4. Magnetic field color maps and arrow representation of flux lines when (I_1, I_2) are a) (1.1, 1.1), b) (2.2, 2.2), c) (4.4, 4.4) and d) (2.2, -2.2) A.

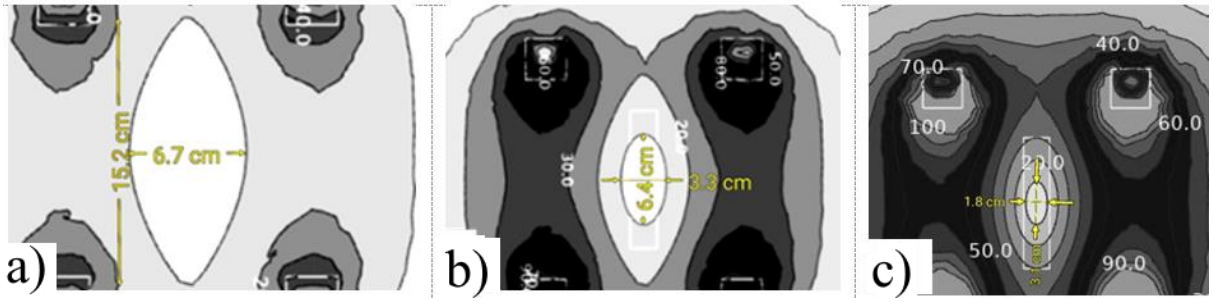

Figure 5. Major and minor axis measurements of FFR when (I_1, I_2) are a) (1.1, 1.1), b) (2.2, 2.2) and c) (4.4, 4.4) A.

3.2. Experiment Results

Measurements were taken at 81 probe locations (see Figure 3b) which are identical with the simulation. Magnetic flux density measurements in the x and y directions (B_x and B_y) were taken for all cases with WT10A magnetic flux meter. The magnitude of the resultant magnetic flux density vector for every point was calculated by Eq. (5),

$$B = \sqrt{B_x^{\,2} + B_y^{\,2}} \tag{5}$$

The magnitude of the vector measurements obtained when (I_1, I_2) were (1.1, 1.1), (2.2, 2.2), (4.4, 4.4) and (2.2, -2.2) A are listed in Table 3. The measurements were repeated 4 times in a row and the average values were transferred to the table. Differences between the simulation environment and experiment setup measurements may be due to ideal conditions in the simulation environment, probe positioning in the experiment setup, measuring device calibration.

Table 3. Magnetic flux density experiment setup measurements.

		(I_1, I_2)= (1.1, 1.1) A									(I_1, I_2)= (4.4, 4.4) A								
B (G)		x-axis probe position (mm)									x-axis probe position (mm)								
		-40	-30	-20	-10	0	10	20	30	40	-40	-30	-20	-10	0	10	20	30	40
y axis probe position	40	16	13	10	10	6	8	12	11	17	58	45	37	30	24	29	38	47	59
	30	13	11	9	7	7	9	10	13	16	53	43	32	25	20	22	32	42	53
	20	15	13	8	7	6	7	7	13	14	49	41	27	18	13	20	27	40	52
	10	13	12	6	4	2	5	9	11	12	50	36	27	17	6	14	27	37	50
	0	12	12	8	4	3	5	9	12	13	50	37	25	12	2	12	25	39	49
	-10	13	11	8	5	2	5	7	11	15	47	38	25	15	6	15	26	37	48
	-20	13	12	8	4	6	4	10	11	15	50	40	27	18	14	18	30	39	50
	-30	16	12	9	8	7	9	10	11	14	55	44	31	24	19	25	34	41	55
	-40	15	11	10	8	8	10	10	11	17	58	46	38	30	25	29	38	46	57
		(I_1, I_2)= (2.2, 2.2) A									(I_1, I_2)= (2.2, -2.2) A								
B (G)		x-axis probe position (mm)									x-axis probe position (mm)								
		-40	-30	-20	-10	0	10	20	30	40	-40	-30	-20	-10	0	10	20	30	40
y axis probe position	**40**	32	23	17	17	13	16	19	23	32	43	39	36	35	34	35	35	38	46
	30	29	22	18	13	11	12	17	23	29	45	40	40	35	37	36	38	39	44
	20	26	19	16	11	9	12	15	20	26	44	42	37	37	36	38	37	40	45
	10	27	18	12	10	3	8	13	19	26	42	40	41	38	38	40	38	42	43
	0	26	19	12	9	1	7	15	21	26	43	41	41	38	37	38	38	40	42
	-10	25	20	15	10	3	7	14	20	26	44	42	38	39	37	37	39	40	43
	-20	26	20	17	11	8	12	16	21	27	42	42	38	38	39	38	40	43	45
	-30	29	24	16	13	11	12	18	23	28	45	39	40	35	36	36	38	42	42
	-40	31	25	20	16	15	15	20	23	32	43	42	36	36	35	36	36	39	45

In agreement with simulation results, if source current gets high, the FFR shrinks in the center and its shape changes from the surface area to a linear form or a point-line form. When (I_1, I_2) are (1.1, 1.1), (2.2, 2.2), (4.4, 4.4), and (2.2, -2.2) A, the number of points creating FFR (red colored regions in Table 3 , B ≤ 10 G) are 44, 11, 3 and 0, respectively.

4. Conclusions

The shape and size compatibility of the FFR with the target object helps localize the heating effect. This highlights the importance of controlling the size and shape of the FFR in MFH applications. However, it appears that the issue of determining FFR characteristics in hyperthermia studies has not been investigated extensively.

In this study, properties of FFR were analyzed in detail with major and minor axis measurements, area calculations and gradient pattern mapping. The obtained results provide data for in vitro and in vivo MFH tests performed prior to clinical trials.

The ability to ablate a tumor of any possible geometry by moving the FFR over the tumor is critical for future studies. FFR and target tissue overlap can be achieved by appropriate placement of the SMF source and/or target object for localized MFH. In the future, designs can be considered to localize the FFR with highly sensitive robotic devices for each patient's unique individual conditions.

Supplementary Material

The point measurements of GPs in simulation medium are available online at https:// docs.google.com/document/d/1CytWgKJinuYSahHmord5I2qhti6WDVC1.

Declaration of Ethical Standards

The author of this article declares that the materials and methods used in this study do not require ethical committee permission and/or legal-special permission.

Conflict of Interest

The author declares that there are no known competing financial interests or personal relationships that could have appeared to influence the work reported in this paper.

References

[1] Huang J., Zhong X., Wang L., Yang L., Mao H., 2012. Improving the magnetic resonance imaging contrast and detection methods with engineered magnetic nanoparticles. Theranostics, **2**, pp. 86–102.

[2] Estelrich J., Sánchez-Martín M.J., Busquets M.A., 2015. Nanoparticles in magnetic resonance imaging: From simple to dual contrast agents. Int. J. Nanomedicine, **10**, pp. 1727–1741.

[3] Arruebo M., Fernández-Pacheco R., Ibarra M.R., Santamaría J., 2007. Magnetic nanoparticles for drug delivery. Nano Today, **2**, pp. 22–32.

[4] Mura S., Nicolas J., Couvreur, P., 2013. Stimuli-responsive nanocarriers for drug delivery. Nat. Mater., **12**, pp. 991–1003.

[5] Mahmoudi K., Bouras A., Bozec D., Ivkov R., Hadjipanayis C., 2018. Magnetic hyperthermia therapy for the treatment of glioblastoma: a review of the therapy's history, efficacy and application in humans. Int. J. Hyperth., **34**, pp. 1316–1328.

[6] Zhao L.-Y., Liu J.-Y., Ouyang W.-W., Li D.-Y., Li L., Li L.-Y., Tang J.-T., 2013. Magnetic-mediated hyperthermia for cancer treatment: Research progress and clinical trials. Chinese Phys. B, **22**, 108104.

[7] Deatsch A.E., Evans B.A., 2014. Heating efficiency in magnetic nanoparticle hyperthermia. J. Magn. Magn. Mater., **354**, pp. 163–172.

[8] Dhavalikar R., Rinaldi C., 2016. Theoretical predictions for spatially-focused heating of magnetic nanoparticles guided by magnetic particle imaging field gradients. J. Magn. Magn. Mater., **419**, pp. 267–273.

[9] Cantillon-Murphy P., Wald L.L., Zahn M., Adalsteinsson E., 2010. Proposing magnetic nanoparticle hyperthermia in low-field MRI. Concepts Magn. Reson. Part A Bridg. Educ. Res., **36**, pp. 36–47.

[10] Tasci T.O., Vargel I., Arat A., Guzel E., Korkusuz P., Atalar E., 2009. Focused RF hyperthermia using magnetic fluids. Med. Phys., **36**, pp. 1906–1912.

[11] Lu Y., Rivera-Rodriguez A., Tay Z.W., Hensley D., Fung K.L.B., Colson C., Saayujya C., Huynh, Q., Kabuli L., Fellows B., 2020. Combining magnetic particle imaging and magnetic fluid hyperthermia for localized and image-guided treatment. Int. J. Hyperth., **37**, pp. 141–154.

[12] Ma M., Zhang Y., Shen X., Xie J., Li Y., Gu N., 2015. Targeted inductive heating of nanomagnets by a combination of alternating current (AC) and static magnetic fields. Nano Res., **8**, pp. 600–610.

[13] Bauer L.M., Situ, S.F., Griswold M.A., Samia A.C.S., 2016. High-performance iron oxide nanoparticles for magnetic particle imaging-guided hyperthermia (hMPI). Nanoscale, **8**, pp. 12162–12169.

[14] Murase K., Takata H., Takeuchi Y., Saito S., 2013. Control of the temperature rise in magnetic hyperthermia with the use of an external static magnetic field. Phys. Medica, **29,** pp. 624–630.

[15] Zhao Q., Wang L., Cheng R., Mao L., Arnold R.D., Howerth E.W., Chen Z.G., Platt S., 2012. Magnetic nanoparticle-based hyperthermia for head & neck cancer in mouse models. Theranostics, **2**, pp. 113–121.

[16] Ristic-Djurovic J.L., Gajic S.S., Ilic A.Z., Romcevic N., Djordjevich D.M., De Luka S.R., Trbovich A.M., Jokic V.S., Cirkovic S., 2018. Design and Optimization of Electromagnets for Biomedical Experiments With Static Magnetic and ELF Electromagnetic Fields. IEEE Trans. Ind. Electron., **65**, pp. 4991–5000.

[17] Ren Z.H., Mu W.C., Huang S.Y., 2019. Design and Optimization of a Ring-Pair Permanent Magnet Array for Head Imaging in a Low-Field Portable MRI System. IEEE Trans. Magn., **55**, pp. 1–8.

[18] Mahadi W.N.L.W., Adi S.R., Nor K.M., 2003. Application of the rare earth permanent magnet in a linear generator driven by an internal combustion engine. In Proceedings of the National Power Engineering Conference, PECon 2003 – Proceedings, pp. 256–261.

[19] Vilas-Boas V., Carvalho F., Espiña B., 2020. Magnetic hyperthermia for cancer treatment: Main parameters affecting the outcome of in vitro and in vivo studies. Molecules, 25.